PPase with Mn(II) in the presence of PCHOHP gives evidence for a strong Mn(II)-Mn(II) interaction with an estimated distance of <7-8 Å, and (3) titration of a PPase-Mn(II)-PCHOHP complex with Ca^{2+} leads to the binding of 1.0 Ca^{2+} per PPase subunit with a loss of the strong Mn(II)-Mn(II) interaction. These observations, taken together with earlier results showing that (a) CaPPi, but not free Ca^{2+}, binds tightly to PPase[35] and (b) PPase binds two Mn(II) ions per subunit in the absence of phosphoryl ligand and three to four Mn(II) ions in the presence of phosphoryl ligand (see above), led us to propose the schematic model for Mn(II) binding to PPase shown in Figure 12B. Here, two Mn(II) ions bind to sites A and B in the absence of phosphoryl ligand and these sites interact only weakly, whereas site C, to which Mn(II) binds in the presence of phosphoryl ligand, has a strong interaction with site A and/or B. According to this model, added Ca^{2+} in the presence of PCHOHP binds uniquely to site C, thus eliminating the strong Mn(II)-Mn(II) interaction.

Subsequently, Knight et al.[8] reported results generally consistent with the model shown in Figure 12B. They studied the effect of Cr(III) and Co(III) complexes of Pi and imidodiphosphate (PNP) on the EPR of enzyme-bound Mn(II) and on the proton relaxation rate of H_2O bound to enzyme-Mn(II). In this work, these authors reported a weak Mn(II)-Mn(II) interaction in the absence of an added phosphoryl ligand (estimated distance 11-14 Å), corresponding to occupancy of sites A and B, a strong Mn(II)-Cr(III) interaction (estimated distances 4.8-5.2 Å for the Pi complex and 7.0-7.5 Å for PNP complexes), corresponding to the site B-site C interaction, and a weaker Mn(II)-Mn(II) interaction in the presence of Co(III) complexes (estimated distance 7-8 Å for the Pi complex and 8-10 Å for the PNP complex), which would indicate that sites A and B are closer together in the presence of a metal ion-phosphoryl ligand complex than in its absence.

The major difference between Cu(II) and Mn(II) binding to PPase, as reflected in Figure 12, is that the two Cu(II) ions bound in the absence of phosphoryl ligand interact with each other more strongly than either does with the Cu(II) bound in the presence of either PCHOHP or of Pi (Figure 12A). These differences between Cu(II) binding and Mn(II) binding may reflect subtle differences in coordination geometry and/or in ligand identity at what are basically the same or largely overlapping sites. Such sites presumably fall within the large active-site cleft found by X-ray crystallographic structural analysis of PPase, which contains at least four divalent metal ion binding sites.[32,33] Alternatively, it is possible that at least some Cu(II) binding to PPase takes place at sites quite distinct from those sites occupied by Mn(II). Our previous studies of Cd^{2+} binding to PPase[7,9] may be relevant in this regard. Cd^{2+}, like Cu(II), confers only very low enzyme activity on PPase. Of the four Cd^{2+} sites per PPase subunit that we observe both by direct binding studies and by ^{113}Cd NMR studies, only two are directly competed for by Mg^{2+}. The other two are believed to bind at sites distinct from the active site. Clearly, additional experiments will be needed in order to distinguish between these two possibilities.

Acknowledgment. We wish to thank Dr. G.H. Reed for sharing his knowledge of EPR with us and Dr. T. Ohnishi for the use of an X-band EPR instrument. This work was supported by NIH Grants AM-13212 to B.S.C. and GM-25052 to J. S. Leigh in the Biochemistry and Biophysics Department.

Registry No. PPase, 9024-82-2; $PCHOHPO_4$, 15468-10-7; Cu, 7440-50-8; PO_4^{3-}, 14265-44-2.

(35) Ridlington, J. W.; Butler, L. G. *J. Biol. Chem.* **1972**, *247*, 7303.

Contribution from the Department of Chemistry, North Carolina State University, Raleigh, North Carolina 27695-8204, and AT&T Bell Laboratories, Murray Hill, New Jersey 07974

Band Electronic Structure of the Molybdenum Blue Bronze $A_{0.30}MoO_3$ (A = K, Rb)

M.-H. Whangbo*[†1a] and L. F. Schneemeyer*[1b]

Received June 7, 1985

The electronic structure of the blue bronze $A_{0.30}MoO_3$ (A = K, Rb) was examined by performing tight-binding band calculations on a number of model chains and an $Mo_{10}O_{30}$ slab. When normalized to $A_3Mo_{10}O_{30}$ (i.e., half the unit cell), the bottom two d-block bands of an $Mo_{10}O_{30}$ slab are partially filled. The Fermi surfaces of these two bands are open along the interchain direction, in agreement with the experimental fact that the blue bronze is a pseudo-one-dimensional metal with good electrical conductivity along the chain direction *b*. The Fermi surfaces of the two bands are curved due to interactions between adjacent $Mo_{10}O_{32}$ chains, but the curvatures of the Fermi surfaces are opposite for the two bands. Thus the two pieces of the first-band Fermi surface are nested to those of the second-band Fermi surface by a single wave vector $q_b \simeq 0.75b^*$, which explains why only one charge density wave occurs in the blue bronze. For an $Mo_{10}O_{30}$ slab, the bottom of the third d-block band is calculated to lie above, but very close to, the Fermi level (i.e., 0.012 eV above e_f). This feature is responsible for the temperature dependence of q_b in the blue bronze, which increases gradually from $\sim 0.72b^*$ at room temperature to $\sim 0.75b^*$ below the metal-to-semiconductor phase-transition temperature.

Solid oxide phases with a range of composition $A_xM_yO_z$ (A = alkali metal, M = transition metal) are generally referred to as bronzes,[2] since they exhibit intense color and metallic luster in most cases. In the $A_xM_yO_z$ bronze, an alkali metal donates its valence electron to the d-block bands of the transition metal. Thus, whether the bronze is a metal or a semiconductor depends upon the nature of its d-block bands. So far three well-defined molybdenum bronzes $A_{0.33}MoO_3$ (A = K), $A_{0.30}MoO_3$ (A = K, Rb) and $A_{0.9}Mo_6O_{17}$ (A = Li, Na, K), have been synthesized and studied. The red bronze[3,4] $A_{0.33}MoO_3$ is a semiconductor at all temperatures,[5] while the purple bronze[3,6] $A_{0.9}Mo_6O_{17}$ is a quasi-two-dimensional (2D) metal.[7]

The blue bronze[3,8] $A_{0.30}MoO_3$ exhibits a metal-to-semiconductor transition at T_c = 180 K,[9] and its electrical properties are strongly anisotropic.[10] On the basis of optical reflectivity data, Travaglini et al.[11] suggested that the blue bronze is a quasi-one-dimensional

[†] Camille and Henry Dreyfus Teacher-Scholar (1980-1985).

(1) (a) North Carolina State University. (b) AT&T Bell Laboratories.
(2) (a) Sienko, M. J. *Nonstoichiometric Compounds*; Gould, R. F., Ed.; American Chemical Society: Washington, DC, 1963; p 224. (b) Hagenmuller, P. *Prog. Solid State Chem.* **1971**, *5*, 71. (c) Wells, A. F. *Structural Inorganic Chemistry*, 5th ed.; Clarendon: Oxford, 1984; p 612. (d) Schlenker, C.; Dumas, J.; Escribe-Filippini, C.; Guyot, H.; Marcus, J.; Fourcaudot, G. *Philos. Mag. B* **1985**, *52*, 643.
(3) Wold, A.; Kunnmann, W.; Arnott, R. J.; Ferretti, A. *Inorg. Chem.* **1964**, *3*, 345.
(4) Stephenson, N. C.; Wadsley, A. D. *Acta Crystallogr.* **1965**, *18*, 241.
(5) Bouchard, G. H.; Perlstein, J. H.; Sienko, M. J. *Inorg. Chem.* **1967**, *6*, 1682.
(6) (a) Stephenson, N. C. *Acta Crystallogr.* **1966**, *20*, 59. (b) Reau, J. M.; Fouassier, C.; Hagenmuller, P. *J. Solid State Chem.* **1970**, *1*, 326. (c) Gatehouse, B. M.; Lloyd, D. J.; Miskin, B. K. *NBS Spec. Publ. (U.S.)* **1972**, *No. 364*, 15. (d) Vincent, H.; Ghedira, M.; Marcus, J.; Mercier, J.; Schlenker, C. *J. Solid State Chem.* **1983**, *47*, 112.

0020-1669/86/1325-2424$01.50/0

Table I. The Exponents ζ_μ and Valence Shell Ionization Potentials $H_{\mu\mu}$ for Slater-Type Orbitals χ_μ[a,b]

χ_μ	ζ_μ	ζ_μ'	$H_{\mu\mu}$, eV
Mo 4d	4.54 (0.6097)	1.90 (0.6097)	−10.5
O 2s	2.275		−32.3
O 2p	2.275		−14.8

[a] The d orbitals of Mo are given as a linear combination of two Slater-type orbitals,[30] and each is followed by weighting factors in parentheses. [b] A modified Wolfsberg–Helmholz formula was used to calculate $H_{\mu\nu}$.[31]

(1D) metal above T_c and the metal-to-semiconductor transition is of Peierls type.[12] Evidence for a charge density wave (CDW) in the blue bronze was later found from the Raman scattering study,[13] and the X-ray diffuse-scattering study of Pouget et al.[14] established that the metal-to-semiconductor transition in the blue bronze is a Peierls transition. This conclusion was confirmed by other X-ray studies[15] and also by neutron[16] and electron[17] diffraction studies.

For the blue bronze, the wave vector component q_b of its CDW is incommensurate at room temperature; i.e., $q_b \simeq 0.72b^*$, where $b^* = 2\pi/b$ and b is the repeat distance along the crystallographic b axis. When the temperature is lowered, the q_b value of the CDW is found to gradually increase. A number of studies on the temperature dependence of q_b shows that it approaches the commensurate value $0.75b^*$ (i.e., $q_b \rightarrow 0.750b^*$,[15,18] $q_b \rightarrow 0.748b^*$,[16,19] $q_b \rightarrow 0.746b^*$,[20] and $q_b \rightarrow 0.749b^*$[21]), although it is not unequivocal whether the blue bronze undergoes a true incommensurate-to-commensurate phase transition[15,18] or not.[16,19-21] This discrepancy might arise from differences in the purity and the stoichiometry of samples investigated. At temperatures below 183 K, nonlinear electrical conductivity attributed to a charge transport by the CDW has been found for the blue bronze.[22-25]

Despite numerous experimental studies on the blue bronze, no band electronic structure calculation has been reported so far except for a very sketchy one by Travaglini and Wachter.[26] The band picture of Travaglini and Wachter is not consistent with the electronic structure of the blue bronze deduced from the optical reflectivity[11] and the X-ray diffuse-scattering[14,21] studies. To gain some insight into the physical properties of the blue bronze, we have carried out band electronic structure calculations on $K_{0.30}MoO_3$ by employing the tight-binding band scheme[27] based upon the extended Hückel method.[28] The atomic parameters used in our calculations are summarized in Table I.

Results and Discussion

A. Structural Model of the Blue Bronze. The blue bronze $A_{0.30}MoO_3$ has 20 formula units per unit cell,[8] and the unit cell $A_6MO_{20}O_{60}$ is large for band structure calculations. It would be a complicated task to unravel how the band electronic structure is related to the crystal structure even if band structure calculations could be performed for the unit cell of this magnitude. Therefore, it is necessary to find a simplified model structure for the blue bronze that captures the essence of the blue bronze structure and is small enough for band structure calculations. Consequently, we first examine how the structure of the blue bronze is assembled from its building blocks, MoO_6 octahedra. While MoO_6 octahedra in the blue bronze are distorted, we will begin our discussion by employing regular MoO_6 octahedra as the building blocks.

The MoO_5 chain **1a** is obtained from MoO_6 octahedra by sharing of their opposite corners. The side and top views of **1a** are given by **1b** and **1c**, respectively. When two MoO_5 chains

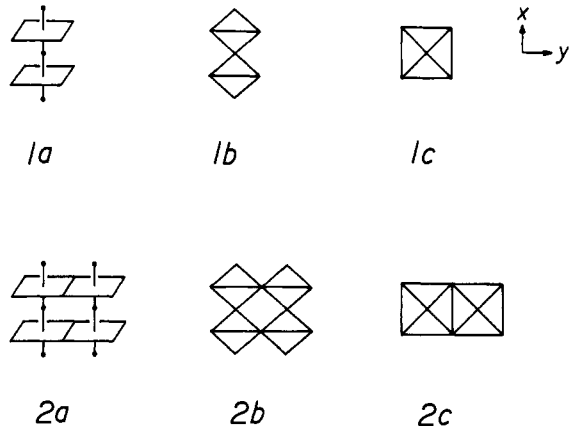

1 are fused together by edge sharing, the Mo_2O_8 chain **2a** results. **2b** and **2c** are the side and top views of **2a**, respectively. For the chains **1** and **2**, the repeat distance is equal to twice the Mo–O distance, $2r_{Mo-O}$. The Mo_5O_{18} chain **3a**, a variation of **2**, is obtained when every Mo_4O_{16} unit of **2** adds an MoO_2 unit to form an extra MoO_6 octahedron. Later in our discussion, this extra MoO_6 octahedron will be referred to as a hump MoO_6 octahedron. Due to the presence of these hump MoO_6 octahedra, the repeat distance of **3a** becomes $4r_{Mo-O}$, twice the repeat distance of **1** or **2**. A side view of **3a** is given by **3b**, while the top view of **3a** may be represented by **3c** or **3d**. The last two differ in their heights along the chain by $2r_{Mo-O}$, half the repeat distance.

The Mo_4O_{14} chain **4a** results from two Mo_2O_8 chains **2** that share edges. Likewise, the $Mo_{10}O_{32}$ chain **4b** is obtained from two Mo_5O_{18} chains **3c** and the $Mo_{10}O_{32}$ chain **4c** from two Mo_5O_{18} chains **3d**. The chains **4b** and **4c** differ in their heights by $2r_{Mo-O}$.

(7) (a) Escribe-Filippini, C.; Konate, K.; Marcus, J.; Schlenker, C.; Almairac, R.; Ayroles, R.; Roucau, C. *Philos. Mag. B* **1984**, *50*, 321. (b) Greenblatt, M.; Ramanujachary, K. V.; McCarroll, W. H.; Neifeld, R.; Waszczak, J. V. *J. Solid State Chem.* **1985**, *59*, 149. (c) Buder, R.; Devenyi, J.; Dumas, J.; Marcus, J.; Mercier, J.; Schlenker, C.; Vincent, H. *J. Phys. Lett.* **1982**, *43*, L59. (d) Greenblatt, M.; McCaroll, W. H.; Neifeld, R.; Croft, M.; Waszczak, J. V. *Solid State Commun.* **1984**, *51*, 671.

(8) (a) Graham, J.; Wadsley, A. D. *Acta Crystallogr.* **1966**, *20*, 93. (b) Ghedira, M.; Chenavas, J.; Marezio, M.; Marcus, J. *J. Solid State Chem.* **1985**, *57*, 300.

(9) (a) Bouchard, G. H.; Perlstein, J. H.; Sienko, M. J. *Inorg. Chem.* **1967**, *6*, 1682. (b) Fogle, W.; Perlstein, J. H. *Phys. Rev. B: Solid State* **1972**, *6*, 1402.

(10) Brusetti, R.; Chakraverty, B. K.; Deveny, Y.; Dumas, J.; Marcus, J.; Schlenker, C. *Recent Developments in Condensed Matter Physics*; Devreese, J. T., Ed.; Plenum: New York, 1981; Vol. 2, p 181.

(11) Travaglini, G.; Watcher, P.; Marcus, J.; Schlenker, C. *Solid State Commun.* **1981**, *37*, 599.

(12) (a) Peierls, R. E. Quantum Theory of Solids; Oxford University Press: London, 1955; p 108. (b) Berlinsky, A. *J. Contemp. Phys.* **1976**, *17*, 331. (c) Whangbo, M. -H. *Acc. Chem. Res.* **1983**, *16*, 95.

(13) Travaglini, G.; Mörke, I.; Wachter, P. *Solid State Commun.* **1983**, *45*, 289.

(14) Pouget, J. P.; Kagoshima, S.; Schlenker, C.; Marcus, J. *J. Phys. Lett.* **1983**, *44*, L113.

(15) Fleming, R. M.; Schneemeyer, L. F.; Moncton, D. E. *Phys. Rev. B: Condens. Matter* **1985**, *31*, 899.

(16) (a) Sato, M.; Fujshita, H.; Hoshino, S. *J. Phys. C.* **1983**, *16*, L877. (b) Sato, N., Fujshita, H.; Hoshino, S. *J. Phys. C.* **1985**, *18*, 2603.

(17) Chen, C. H.; Schneemeyer, L. F.; Fleming, R. M. *Phys. Rev. B: Condens. Matter* **1984**, *29*, 3765.

(18) (a) Fleming, R. M.; Schneemeyer, L. F. *Bull. Am. Phys. Soc.* **1984**, *29*, 470. (b) Dieker, S. B.; Lyons, K. B.; Schneemeyer, L. F. *Bull. Am. Phys. Soc.* **1984**, *29*, 469.

(19) Escribe-Filippini, C.; Pouget, J. P.; Currat, R.; Hennion, B.; Marcus, J. *Lect. Notes Phys.* **1985**, *217*, 71.

(20) Tamegai, T.; Tsutsumi, K.; Kagoshima, S.; Kanai, Y.; Tani, M.; Tomozawa, H.; Sato, M.; Tsuji, K.; Harada, J.; Sakata, M.; Nakajima, T. *Solid State Commun.* **1984**, *51*, 585.

(21) Pouget, J. P.; Noguera, C.; Moudden, A. H.; Moret, T. *J. Phys.* (*Les Ulis, Fr.*) **1985**, *46*, 1731.

(22) (a) Dumas, J.; Schlenker, C.; Marcus, J.; Buder, R. *Phys. Rev. Lett.* **1983**, *50*, 757. (b) Schlenker, C.; Dumas, J. *Crystal Structures and Properties of Materials with Quasi One-Dimensional Structures*: Rouxel, J., Ed.; Reidel: Dordrecht, The Netherlands, 1986.

(23) Schlenker, C.; Filippini, C.; Marcus, J.; Dumas, J.; Pouget, J. P.; Kagoshima, S. *J. Phys.* (*Les Ulis, Fr.*) **1983**, *44*, C3-1757.

(24) Schneemeyer, L. F.; DiSalvo, F. J.; Fleming, R. F.; Waszczak, J. V. *J. Solid State Chem.* **1984**, *54*, 538.

(25) (a) Dumas, J.; Schlenker, C. *Solid State Commun.* **1983**, *45*, 885. (b) Fleming, R. M.; Schneemeyer, L. F. *Phys. Rev. B: Condens. Matter* **1983**, *28*, 6996.

(26) Travaglini, G.; Wachter, P. *Lect. Notes Phys.* **1985**, *217*, 71.

(27) (a) Whangbo, M.-H.; Hoffmann, R. *J. Am. Chem. Soc.* **1978**, *100*, 6093. (b) Whangbo, M.-H.; Hoffmann, R.; Woodward, R. B. *Proc. R. Soc. London, Ser. A* **1979**, *366*, 23.

(28) Hoffmann, R. *J. Chem. Phys.* **1963**, *39*, 1397.

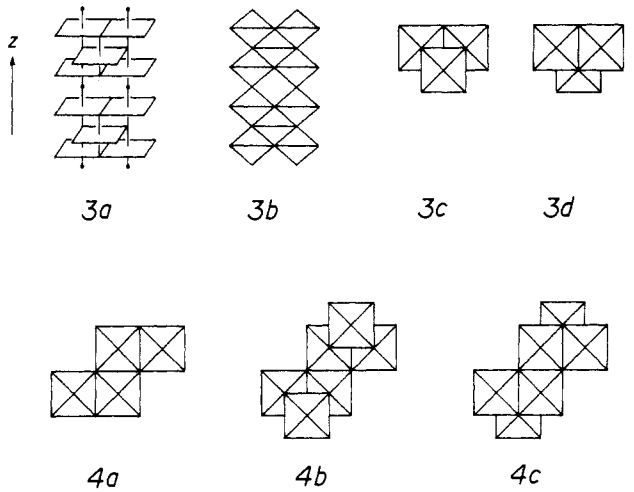

The 2D $Mo_{10}O_{30}$ slab in **5** is constructed from the $Mo_{10}O_{32}$ chains

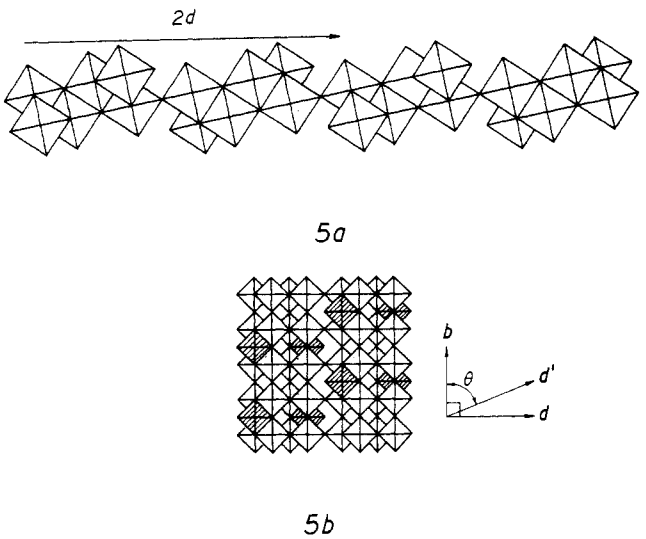

4b and **4c** by corner sharing. Given the primitive vectors of an $Mo_{10}O_{30}$ slab as b and d' (see **5a** and **5b**), the chains **4b** and **4c** alternate in interchain direction $d = d' - b/2$ (perpendicular to the chain direction b) as shown in **5a**, a projected view of an $Mo_{10}O_{30}$ slab along b. Shown in **5b** is a projected view of an $Mo_{10}O_{30}$ slab along the interslab direction, where the hump MoO_6 octahedra are shaded for the purpose of clarity. The blue bronze $A_{0.30}Mo_{10}O_{30}$ consists of $Mo_{10}O_{30}$ slabs such as **5**, which are separated by alkali ions A^+ to give $A_6Mo_{20}O_{60}$ as the unit cell (i.e., two $Mo_{10}O_{30}$ slabs per unit cell). In the so-called C-centered unit cell of Graham and Wadsley,[8] each $Mo_{10}O_{30}$ slab of the blue bronze is contained in a plane defined by the two orthogonal vectors b and $2c + a$. In **5** the plane of each $Mo_{10}O_{30}$ slab is defined either by the two orthogonal vectors b and d or by the two nonorthogonal vectors b and d'. It is noted that $2d = 2c + a$.

If alkali-metal atoms were absent from the blue bronze $A_{0.30}MoO_3$, its d-block bands would be empty due to the formal oxidation states of Mo^{6+} (d^0) and 3 O^{2-} for MoO_3. Thus the electrons donated from alkali-metal enter the d-block bands. Since the unit cell is $A_6Mo_{20}O_{60}$, six electrons per unit cell fill the d-block bands, which consist of 100 bands. This leads to a few partially filled d-block bands, which are responsible for the quasi-1D metallic properties of the blue bronze above T_c. The interactions between the $Mo_{10}O_{30}$ slabs in the blue bronze are weak so that the band structure of the blue bronze may be approximated by that of a 2D $Mo_{10}O_{30}$ slab. As noted from **5**, a 2D $Mo_{10}O_{30}$ slab is constructed from 1D $Mo_{10}O_{32}$ chains **4b** and **4c** upon corner sharing. If the interactions between adjacent $Mo_{10}O_{32}$ chains of an $Mo_{10}O_{30}$ slab are small, the band electronic structure of the blue bronze may also be approximated by that of a 1D $Mo_{10}O_{32}$

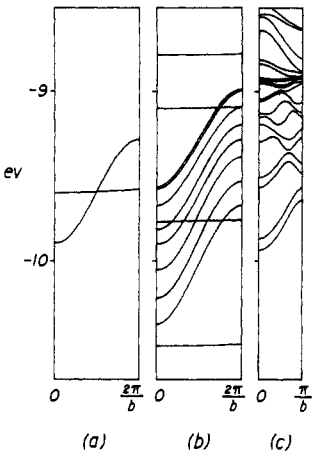

Figure 1. Low-lying d-block bands calculated for (a) the ideal MoO_5 chain **1**, (b) the ideal Mo_4O_{14} chain **4a**, and (c) the real Mo_8O_{28} chain **4a**.

chain. For an $Mo_{10}O_{32}$ chain and an $Mo_{10}O_{30}$ slab, we need to put three electrons into their d-block bands to simulate the Fermi level of the blue bronze.

B. Band Structure. 1. $Mo_{10}O_{32}$ Chain. To examine how the band electronic structure is related to the crystal structure in the blue bronze, we have calculated the band electronic structures of the chains **1**, **4a**, and **4b**. These chains will be referred to as ideal chains if they are constructed from regular MoO_6 octahedra (with r_{Mo-O} = 2.0 Å, the average Mo–O distance in the blue bronze) and as real chains if they are constructed from distorted MoO_6 octehedra as found in the room-temperature crystal structure of the blue bronze.[8]

Each Mo atom of ideal chain **1** is octahedrally coordinated, so the d-block bands of ideal **1** will have three bands derived from the t_{2g} level of Mo (i.e., t_{2g} subbands) lying below two bands derived from the e_g level of Mo (i.e., e_g subbands). Figure 1a shows the t_{2g} subbands of ideal **1**, where $b = 4r_{Mo-O}$. With the z axis taken along the chain and the x and y axes as in **1c**, the t_{2g} subbands consist of a nearly flat σ band (i.e., $x^2 - y^2$ band) and doubly degenerate π bands (i.e., xz, yz bands).

Figure 1b shows the t_{2g} subbands of ideal **4a**, which are comprised of eight π bands derived from xz, yz orbitals and four flat σ bands derived from $x^2 - y^2$ orbitals. All the π bands are nondegenerate, and the lowest-lying σ band lies below the bottom of the π bands. In the lowest-lying σ band, four $x^2 - y^2$ orbitals in every metal atom plane (perpendicular to the chain) are combined in-phase as shown in **6**.

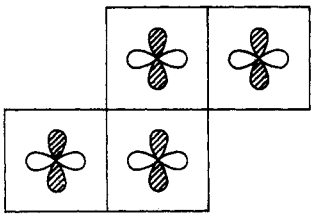

6

The repeat distance of real chain **4b** is aproximately given by the $4r_{Mo-O}$ value of ideal chains. Removal, from real **4b**, of MoO_2 units that make up the hump MoO_6 octahedra leads to real **4a**. The repeat distance of real **4a** is the same as that of real **4b**. Figure 1c shows the low-lying d-block bands of real **4a**, which is essentially a modified version of the band structure obtained from Figure 1b when the second half of this band is folded onto the first half. Important features of Figure 1c are summarized as follows: (a) A pair of π bands, which are close in energy, are the lowest-lying bands of the whole d-block bands. This is a direct consequence of the distortion in MoO_6 octahedra. **7a** shows a view of the Mo and O atom positions of real **4a** projected along the chain.

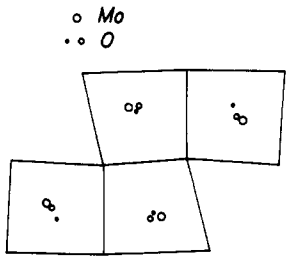

7a

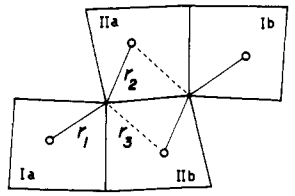

7b

Compared with those in ideal **4a**, the metal–metal distance between neighboring MoO_6 octahedra are increased in real **4a** so that a good σ-bonding orbital such as **6** cannot be formed in real **4a**. In additlon, **7a** shows that a metal atom within each tetragon of four "equatorial" oxygen atoms has a short distance to one oxygen atom. This leads to a strong interaction between the metal and the oxygen, which lowers the energy of the p-block bands associated with such oxygen atoms but raises the σ d-block bands of primarily $x^2 - y^2$ orbitals. The π bands of real **4a** are raised in energy compared with those of ideal **4a**. As shown in **7a**, the Mo and "axial" O atoms of each Mo–O linkage along the chain are not contained in a plane. Such a distortion from the structure of ideal **4a** enhances the π interactions between Mo and axial O atoms.[29] This lowers the p-block bands of axial oxygen atoms (of largely x, y orbitals in nature) but raises the π d-block bands of primarily xz, yz orbitals. (b) The π bands occur in pairs in real **4a**, which has an important consequence on the electrical properties of the blue bronze as will be discussed later. As shown in **7b**, real chain **4a** may be considered in terms of two "outer" subchains (Ia and Ib) and two "inner" subchains (IIa and IIb). In **7b** there are two oxygen atoms common to three subchains that might be referred to as the intersection oxygen atoms. The Mo atoms of different subchains interact with one another via those intersection oxygen atoms. The three Mo–O distances r_1, r_2, and r_3 are related as $r_2 < r_1 \ll r_3$ (i.e., $r_2 \simeq 1.89$ Å, $r_1 \simeq 1.97$ Å, and $r_3 \simeq 2.32$ Å). Therefore subchain Ia interacts strongly with IIa but weakly with IIb. Likewise, subchain Ib interacts strongly with IIb but weakly with IIa. In other words, in real **4a**, a pair of strongly interacting subchains Ia and IIa interact weakly with a pair of strongly interacting subchains Ib and IIb. At the zone center the lowest-lying pair of π bands is constructed from the orbitals **8a** and **8b**. The metal orbitals of **8** are combined out-

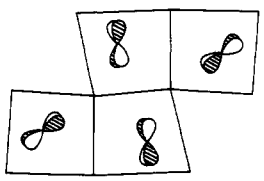

8a

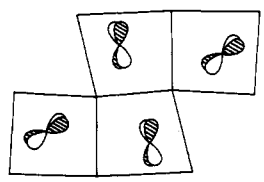

8b

of-phase between Ia and IIa and between Ib and IIb, so that there is no z-orbital contribution from the intersection oxygen atoms in **8**. The pair of Ia and IIa interact with that of Ib and IIb in-phase in **8a** but out-of-phase in **8b**, so that **8a** and **8b** refer to the lower and the upper bands of the lowest-lying pair of π bands, respectively. At the zone center the pair of π bands lying just above the lowest-lying pair are constructed from the orbitals **9a** and **9b**. The metal orbitals of **9** are combined in-phase between Ia and IIa and between Ib and IIb, so that z orbitals of the intersection oxygen atoms combine out-of-phase with the metal orbitals of Ia and IIa and with those of Ib and IIb. Thus the

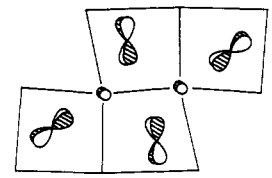

9a

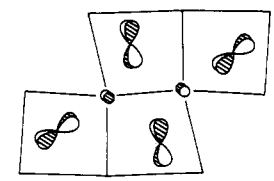

9b

orbitals **9a** and **9b** lie higher in energy than the orbitals **8a** and **8b**. The pair of Ia and IIa interact with that of Ib and IIb in-phase in **9a** but out-of-phase in **9b**, so that **9b** lies higher in energy than **9a**. Note form Figure 1c that the energy difference between **8** and **9** is much greater than that between **8a** and **8b** or that between **9a** and **9b**. This is due to the fact that $r_2 < r_1 \ll r_3$, which explains why the π bands occur in pairs for a real $Mo_{10}O_{32}$ chain.

The low-lying d-block bands of real **4b** are shown in Figure 2b, and for the purpose of comparison, those of real **4a** are shown in Figure 2a. For those bands, real **4b** is nearly identical with real **4a** since the metal d orbitals of the hump octahedra contribute little to the low-lying d-block bands of real **4b**. This conclusion has also been reached from X-ray diffraction study of Ghedira et al.[8b] Thus our discussion of real **4a** concerning why the π d-block bands occur in pairs is valid for real chain **4b**. Upon the structural change ideal **4b** → real **4b**, the metal d-block and the oxygen p-block bands are raised and lowered in energy, respectively. However, according to our calculations, real **4b** is more stable than ideal **4b** by more than 1 eV/Mo. For real **4b**, the top of the oxygen p-block bands is calculated to be ~4.5 eV below the bottom of the d-block bands, in reasonable agreement with the optical reflectivity peak at 3.7 eV[13] In Figure 1c a number of nearly flat bands lie ~1 eV above the bottom of the d-block bands. The same is observed in the band structure of real **4b**, though not shown in Figure 2b. This group of flat bands would be responsible for the optical reflectivity peak at 4.5 eV (i.e., ~0.8 above the 3.7-eV peak).[13] With three electrons per unit cell to fill the d-block bands of Figure 2b, the low-lying d-block bands become roughly three-fourths filled. The Fermi wave vectors of the two bands (i.e., wave vectors corresponding to the Fermi level e_f) are $k_f = 0.33b^*$ and $k_f' = 0.42b^*$.

2. $Mo_{10}O_{30}$ Slab. Figure 3 shows two Brillouin zones of an $Mo_{10}O_{30}$ slab that result from the two sets of vectors defined in **5b**. The set of nonorthogonal vectors b and d' leads to the hexagonal Brillouin zone, while that of orthogonal vectors b and d leads to the rectangular Brillouin zone. Here $|\Gamma X| = |\Gamma X'| \sin\theta$, so that the areas of the two Brillouin zones are the same. In our study, the band electronic structures and the Fermi surfaces of a real $Mo_{10}O_{30}$ slab were calculated upon the basis of the wave vectors of the hexagonal Brillouin zone. However, in describing the Fermi surfaces, it is convenient to employ the rectangular Brillouin zone, since $|\Gamma X|$ is equal to $b^*/2$ of the blue bronze crystal and since the experimental q_b wave vector is defined along the direction $\Gamma \rightarrow X$.

Shown in Figure 4 are the bottom four d-block bands of a real $Mo_{10}O_{30}$ slab (as found for the room-temperature crystal structure[8b]) calculated along the directions $\Gamma \rightarrow X'$ and $\Gamma \rightarrow Y'$ of the hexagonal Brillouin zone. As in the case of a real $Mo_{10}O_{32}$ chain, the low-lying bands of Figure 4 are largely π bands of Mo atoms of inner and outer subchains (Ia, Ib, IIa, IIb) in orbital character. The lowest two π bands cross the Fermi level along the chain direction ($\Gamma \rightarrow X'$), and their dispersion is small along the interchain direction ($\Gamma \rightarrow Y'$). Thus a real $Mo_{10}O_{30}$ slab is expected to be pseudo-one-dimensional in its electrical properties, but it is noted from Figures 2 and 4 that the low-lying π bands of a real $Mo_{10}O_{30}$ slab do not occur in pairs in contrast to the case of a real $Mo_{10}O_{32}$ chain. This originates from the fact that interactions between adjacent $Mo_{10}O_{32}$ chains of the slab, which occur via Mo(Ia)–O–Mo(Ib) linkages (see **10**), are substantial. The Mo–O distance r_4 of such a linkage is rather short (i.e., 1.89 Å). Since $r_4 \simeq r_2 < r_1$, the interaction between subchains Ia and Ib of two adjacent $Mo_{10}O_{32}$ chains is stronger than that between subchains Ia and IIa (or Ib and IIb) of an $Mo_{10}O_{32}$ chain as far as the bottom

(29) Whangbo, M.-H. *Crystal Chemistry and Properties of Materials with Quasi One-Dimensional Structures*; Rouxel, J., Ed.; Reidel: Dordrecht, The Netherlands, 1986; p 27.
(30) Basch, H.; Viste, A.; Grey, H. B. *Theor. Chim. Acta* **1965**, *3*, 458.
(31) Ammeter, J. H.; Bürgi, H.-B.; Thibeault, J. C.; Hoffmann, R. *J. Am. Chem. Soc.* **1978**, *100*, 3686.

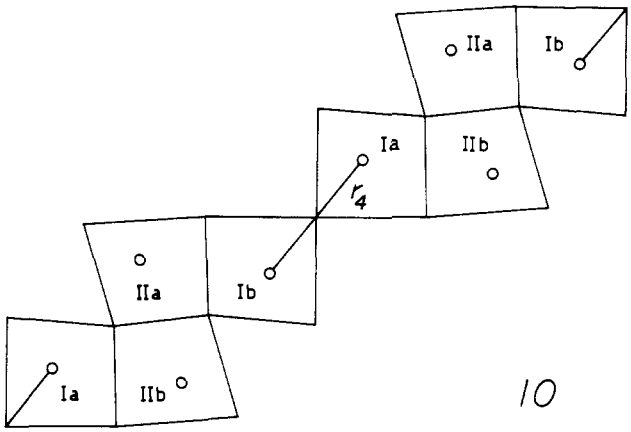

portion of the d-block bands are concerned. Thus the first and fourth band of Figure 4 (from the bottom) have stronger outer-subchain (Ia, Ib) character whereas the second and third bands have stronger inner-subchain (IIa, IIb) character.

With three electrons per unit cell (normalized to $A_3Mo_{10}O_{30}$) to put in the d-block bands of Figure 4, the Fermi level e_f is calculated to be only 0.012 eV below the bottom of the third band. This feature of the band electronic structure is crucial in explaining the temperature dependence of q_b, as recently shown by Pouget et al.[21] The Fermi surfaces calculated for the first and second bands of Figure 4 are shown in parts a and b, respectively, of Figure 5, where we employed the rectangular Brillouin zone of Figure 3. The Fermi surfaces of the two bands are open, so that the blue bronze is predicted to be 1D metallic in agreement with experiment. Due to interactions between $Mo_{10}O_{32}$ chains along the interchain direction of an $Mo_{10}O_{30}$ slab, the Fermi surfaces of the two bands are curved. The two bands have opposite senses of curvature in their Fermi surfaces, as proposed by Pouget et al.,[21] which originate essentially from the fact that, as one goes from Γ to X in Figure 4, the first band is lowered in energy but the second band is raised in energy. Consequently, as illustrated in Figure 5c, the upper Fermi surface of the first band is nested to the lower Fermi surface of the second band by the wave vector $q_b = 0.75b^*$ and so is the lower Fermi surface of the first band to the upper Fermi surface of the second band. This explains why there occurs only one CDW in the blue bronze, as suggested by Pouget et al.[21]

Given the two partially filled d-block bands nested by an identical wave vector q_b, the total number of electrons n in the two bands is given by $n = 4q_b/b^*$. The temperature dependence of q_b, which increases from $\sim 0.72b^*$ at room temperature to $\sim 0.75b^*$ below T_c, has been explained by Pouget et al.[21] by supposing that a flat band lies above, but very close to, the Fermi level e_f. In such a case, population of the flat band by thermal excitation from the two partially filled bands would lead to a smaller q_b value for the latter. Thus, if the flat band lies at e_0, the total number of electrons n is given by

$$n = 4q_b/b^* + 2/\{\exp[(e_0 - e_f)/kT] + 1\}$$

Pouget et al.[21] found this equation in excellent agreement with the observed q_b values when the $e_0 - e_f$ value is taken to be 0.056 eV. Our calculations of 2D real slab $Mo_{10}O_{30}$ (Figure 4) show that the bottom of the third band lies 0.012 eV above e_f, a value much smaller than 0.056 eV. This result is expected, since the third d-block band of the blue bronze is not flat as shown in Figure 4: Given a pseudo-1D band, its density of state is high at the bottom and at the top of the band. Since the bottom of the third band lies below the top of either the first or the second band, thermal excitation from the bottom two bands will primarily populate the bottom portion of the third band. Thus, the "flat band" model of Pouget et al.[21] is consistent with the results of our band electronic structure calculations.

Concluding Remarks

To unravel the essential features of the band electronic structure of the blue bronze $A_{0.30}MoO_3$ (A = K, Rb), tight-binding band calculations were performed on a series of model chains and on an $Mo_{10}O_{30}$ slab found in the room-temperature structure of the blue bronze.[8b] Each $Mo_{10}O_{30}$ slab of the blue bronze is made up of $Mo_{10}O_{32}$ chains that share corner oxygen atoms and thus interact via Mo(Ia)–O–Mo(Ib) linkages. Our calculations reveal that the low-lying d-block bands of the blue bronze are π bands.

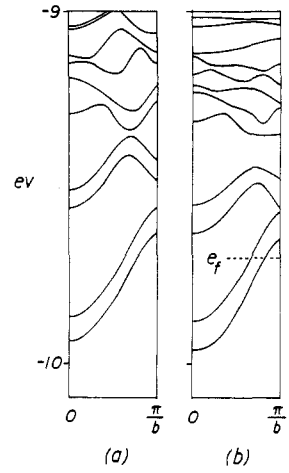

Figure 2. Low-lying d-block bands calculated for (a) the real Mo_8O_{28} chain **4a** and (b) the real $Mo_{10}O_{32}$ chain **4b**.

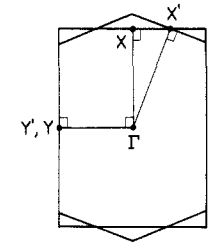

Figure 3. Brillouin zones associated with the two sets of vectors defining the plane of the real $Mo_{10}O_{30}$ slab **5b**: (a) hexagonal Brillouin zone for the nonorthogonal vectors b' (i.e., b) and d', where $X' = (b'^*/2, 0)$ and $Y' = (0, d'^*/2)$; (b) tetragonal Brillouin zone for the orthogonal vectors b and d, where $X = (b^*/2, 0)$ and $Y = (0, d^*/2)$. Note that $b^* = b'^* \sin\theta$, where θ is the angle between b' and d'.

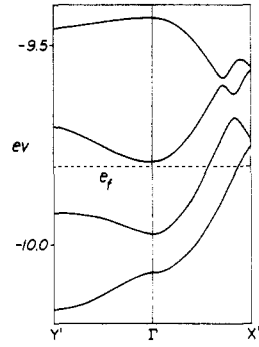

Figure 4. The bottom four d-block bands calculated for the real $Mo_{10}O_{30}$ slab **5** along the $\Gamma \rightarrow X'$ and $\Gamma \rightarrow Y'$ directions of the hexagonal Brillouin zone, where the dashed line refers to the Fermi level.

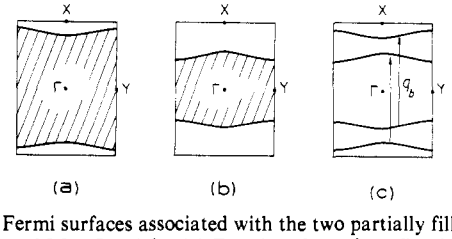

Figure 5. Fermi surfaces associated with the two partially filled d-block bands of a real $Mo_{10}O_{30}$ slab: (a) Fermi surface of the first band, where the wave vectors of the shaded and unshaded regions lead to occupied and unoccupied band levels, respectively; (b) Fermi surface of the second band; (c) nesting of the Fermi surfaces of the first and second bands.

For a real $Mo_{10}O_{32}$ chain, these π bands occur in pairs since the pair of subchains Ia and IIa interact weakly with that of subschains Ib and IIb. When normalized to $A_3Mo_{10}O_{30}$ (half the unit cell of the blue bronze), the bottom two d-block bands become roughly three-fourths filled. This simple picture of the electronic structure of the blue bronze is modified somewhat for a real $Mo_{10}O_{30}$ slab, because the interaction between subchains Ia and Ib via the Mo(Ia)–O–Mo(Ib) linkage of two adjacent $Mo_{10}O_{32}$ chains is stronger than that between subchains Ia and IIa (or Ib and IIb) within an $Mo_{10}O_{32}$ chain. Thus for an $Mo_{10}O_{30}$ slab, the first and fourth d-block bands (from the bottom) have stronger outer subchain (Ia, Ib) character whereas the second and third bands have stronger inner subchain (IIa, IIb) character. Nevertheless, the bottom two d-block bands of a real $Mo_{10}O_{30}$ slab become partially filled with three electrons for the d-block bands per $A_3Mo_{10}O_{30}$. The upper and lower Fermi surfaces of the first band are found to be nested to the lower and upper Fermi surfaces of the second band, respectively, by the identical wave vector $q_b = 0.75b^*$. This explains why there occurs a single CDW in the blue bronze, as proposed by Pouget et al.[21] For a real $Mo_{10}O_{30}$ slab, the third d-block band lies only 0.012 eV above the Fermi level. Thus, population of the bottom of the third band by thermal excitation from the bottom two bands will decrease the q_b value of the latter bands. As shown by Pouget et al.,[21] this accounts for the temperature dependence of q_b in the blue bronze, which increases gradually from $\sim 0.72b^*$ at room temperature to $\sim 0.75b^*$ below T_c.

Acknowledgment. This work was in part supported by the Dreyfus Foundation through a Teacher-Scholar Award to M.-H.W., who is deeply indebted to Dr. J. P. Pouget, Dr. C. Noguera, and Professor C. Schlenker for invaluable discussions and references. M.-H.W. and L.F.S. wish to thank Dr. R. M. Fleming, Dr. F. J. DiSalvo, and Dr. P. Littlewood for valuable comments. M.-H.W. is thankful to G. A. Long for his computational help at the initial stage of this work.

Contribution from the Department of Chemistry,
Iowa State University, Ames, Iowa 50011

Variable-Temperature ^{195}Pt NMR Spectroscopy, a New Technique for the Study of Stereodynamics. Sulfur Inversion in a Platinum(II) Complex with Methionine

David D. Gummin, Eva Marie A. Ratilla, and Nenad M. Kostić*

Received February 12, 1986

This paper introduces ^{195}Pt NMR spectroscopy as a method for the study of stereodynamics and apparently represents only the third report on variable-temperature ^{195}Pt NMR spectroscopy. Displacement of a Cl^- ligand from $PtCl_4^{2-}$ by *N*-acetyl-L-methionine (AcMetH) yields $[Pt(AcMetH)Cl_3]^-$ (**1**), which is a model for the binding of $PtCl_3^-$ label to proteins. The complex in solution is characterized by the method of preparation and by its UV–vis and ^1H, ^{13}C, and ^{195}Pt NMR spectra. The AcMetH ligand is coordinated to the Pt(II) atom through the S atom in the side chain; coordination of the amide N atom, which would result in a six-membered ring, does not occur. We conclude that the coordination of the amide nitrogen to platinum is facilitated if it yields a five-membered ring or a larger chelate containing such a ring. On account of its chiral S atom, complex **1** exists in two diastereomeric forms, which are undetectable in the ^1H and ^{13}C NMR spectra at convenient temperatures but are clearly evident in the ^{195}Pt NMR spectrum. The ^{195}Pt NMR spectra at nine temperatures spanning 86 deg show reversible, intramolecular inversion of configuration at the S atom; $\Delta G^* = 63.7$ kJ mol^{-1} at 335 K. Other mechanisms for the interconversion of the diastereomers are ruled out. Since the chiral carbon and sulfur atoms are three bonds apart, there is virtually no stereochemical discrimination and the two diastereomers of **1** exist in equal concentrations. This finding is discussed in terms of the known molecular structures of methionine and its derivatives. We point out that ^{195}Pt NMR spectroscopy is uniquely suited to the study of dynamic processes involving relatively complex biomolecules and processes causing subtle changes in molecular structure.

Introduction

Selective binding of metal complexes to proteins and other biological macromolecules opens various possibilities for the study of these macromolecules. Suitable metals that are covalently attached to protein surfaces can serve as spectroscopic probes of structure and dynamics, redox probes of electron-transfer reactivity, anomalous scatterers for X-ray crystallography, and modifiers of drug action. We have shown[1] that the chloro(2,2′:6′,2″-terpyridine)platinum(II) complex, $[Pt(trpy)Cl]^+$, possesses the required stability, reactivity, and spectroscopic properties to be a useful labeling reagent for selected histidine, cysteine, and arginine residues in cytochromes *c* from horse, tuna, and baker's yeast. These studies in our laboratory were prompted by an earlier discovery that the $PtCl_4^{2-}$ complex binds covalently to exposed methionine residues in proteins[2] and by the subsequent widespread use of this complex as a heavy-atom label for X-ray determination of protein structure.[3,4] Our ultimate goal is to apply ^{195}Pt NMR spectroscopy to platinum-labeled proteins and study the motions of the flexible side chains of amino acid residues at the protein surface. Since the ^{195}Pt NMR signal of a platinum atom bonded to a biological macromolecule has never been observed,[4,5] we first studied the complex $[Pt(AcMetH)Cl_3]^-$ (**1**; AcMetH = *N*-acetyl-L-methionine). This complex is a model

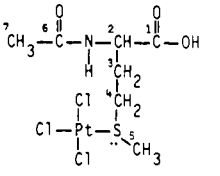

1

for the attachment of the $PtCl_3^-$ label to the side chain of the methionine residue in proteins. Relatively few amino acid complexes of platinum are known,[6–9] and like those of other metals,

(1) Ratilla, E. M. A.; Brothers, H. M., II; Kostić, N. M., unpublished work.
(2) Dickerson, R. E.; Eisenberg, D.; Varnum, J.; Kopka, M. L. *J. Mol. Biol.* **1969**, *45*, 77–84.
(3) Petsko, G. A.; Phillips, D. C.; Williams, R. J. P.; Wilson, I. A. *J. Mol. Biol.* **1978**, *120*, 345–359.
(4) Howe-Grant, M. E.; Lippard, S. J. *Met. Ions Biol. Syst.* **1980**, *11*, 63–125.
(5) Ismail, I. M.; Sadler, P. J. *ACS Symp. Ser.* **1983**, *No. 209*, 171–190.
(6) Volshtein, L. M. *Sov. J. Coord. Chem. (Engl. Transl.)* **1976**, *1*, 483–509 and references cited therein.
(7) McAuliffe, C. A.; Murray, S. G. *Inorg. Chem. Acta, Rev.* **1972**, *6*, 103–121, 111–114.

0020-1669/86/1325-2429$01.50/0